Strongly turbulent Rayleigh–Bénard convection in mercury: comparison with results at moderate Prandtl number

By S. CIONI, S. CILIBERTO and J. SOMMERIA

Ecole Normale Supérieure de Lyon, Laboratoire de Physique, 46, Allée d'Italie, 69364 Lyon Cedex 07, France

An experimental study of Rayleigh–Bénard convection in the strongly turbulent regime is presented. We report results obtained at low Prandtl number (in mercury, $Pr = 0.025$), covering a range of Rayleigh numbers $5 \times 10^6 < Ra < 5 \times 10^9$, and compare them with results at $Pr \sim 1$. The convective chamber consists of a cylindrical cell of aspect ratio 1.

Heat flux measurements indicate a regime with Nusselt number increasing as $Ra^{0.26}$, close to the 2/7 power observed at $Pr \sim 1$, but with a smaller prefactor, which contradicts recent theoretical predictions. A transition to a new turbulent regime is suggested for $Ra \simeq 2 \times 10^9$, with significant increase of the Nusselt number. The formation of a large convective cell in the bulk is revealed by its thermal signature on the bottom and top plates. One frequency of the temperature oscillation is related to the velocity of this convective cell. We then obtain the typical temperature and velocity in the bulk versus the Rayleigh number, and compare them with similar results known for $Pr \sim 1$.

We review two recent theoretical models, namely the mixing zone model of Castaing *et al.* (1989), and a model of the turbulent boundary layer by Shraiman & Siggia (1990). We discuss how these models fail at low Prandtl number, and propose modifications for this case. Specific scaling laws for fluids at low Prandtl number are then obtained, providing an interpretation of our experimental results in mercury, as well as extrapolations for other liquid metals.

1. Introduction

Rayleigh–Bénard convection occurs in a horizontal layer of fluid subjected to uniform heating from below and cooling from above. The dynamics depends on the Rayleigh number Ra and Prandtl number Pr:

$$Ra = \frac{g\alpha\Delta L^3}{\nu\kappa}, \tag{1.1}$$

$$Pr = \nu/\kappa, \tag{1.2}$$

where α is the thermal expansion coefficient, ν the kinematic viscosity, κ the thermal diffusivity, Δ is the temperature difference between the bottom and top plates, and L is the fluid layer height.

We study here the strongly turbulent regime, obtained at high Rayleigh numbers.

The subject has a long history, but interest has been recently renewed by experimental and theoretical developments (see Siggia 1994 for a review). Early experiments were reasonably well interpreted by a mixing length theory, put in a final form by Kraichnan (1962). Scaling laws $Nu \sim Ra^{1/3}$ for $Pr > 0.1$ and $Nu \sim (Ra\,Pr)^{1/3}$ for $Pr < 0.1$ were predicted. In fact the experimental exponent for Nu versus Ra was found to be slightly smaller than $1/3$, and this discrepancy was clearly established by Threlfall (1975) using helium gas at low temperature (which allows a wide range of Ra in a single experimental cell). Castaing *et al.* (1989) repeated similar experiments, and in addition found scaling laws for turbulent fluctuations. They have proposed a model of the mixing zone (see §5.4) explaining their experimental findings, among which is a scaling law $Nu \sim Ra^{2/7}$. Shraiman & Siggia (1992) proposed an alternative model providing essentially the same results from different hypotheses (see §5.2).

In this context, it is important to study what happens at low Prandtl number. This case was investigated long ago by Globe & Dropkin (1959) and Rossby (1969), but measurements were limited to global heat transfers at moderate Rayleigh numbers. Cioni, Ciliberto & Sommeria (1996) have performed similar heat transfer measurements in mercury at higher Rayleigh numbers (5×10^6–5×10^9). These results are reviewed in §3, and compared with results for liquids at different Pr. It appears that for $Ra < 4.5 \times 10^8$, the experimental results are well fitted by a law $Nu \sim Ra^{2/7}$, but with a lower prefactor than for $Pr \sim 1$, while new regimes are obtained beyond $Ra = 4.5 \times 10^8$.

Cioni *et al.* (1996) also found that convection in the bulk is spontaneously organized into a large convective cell. This global circulation was detected by the temperature anomaly that it induces on the bottom and top plates. It appears to change in orientation over long time scales, a fact not previously noted in other liquids. In §4 we characterize these fluctuations in more detail, showing that the global circulation remains remarkably well organized while it fluctuates in orientation and amplitude.

Turbulent temperature fluctuations in the bulk have been analysed in the same mercury experiment by Cioni, Ciliberto & Sommeria (1995): small-scale fluctuations behave like a passive scalar in ordinary (Kolmogorov) turbulence (i.e. they are transported by the flow without influence on the dynamics), although the large scales are of course actively driven by buoyancy. For moderate Pr, temperature appears by contrast to be active at small scales, according to the dynamics of Bolgiano–Oboukhov. We further discuss this difference in Appendix A.

Takeshita *et al.* (1996) have performed similar convection experiments in mercury, also using a cylindrical cell with aspect ratio 1, but with a smaller size, and therefore smaller Ra (in the range 10^6–10^8). They have confirmed a law $Nu \sim Ra^{2/7}$ with a lower prefactor than for $Pr \sim 1$. In addition they have measured how the global circulation velocity scales versus Ra, finding a law similar to experiments at $Pr \sim 1$. They have detected an oscillation frequency associated with this global circulation, scaling like the velocity, as observed for $Pr \sim 1$ (Sano, Wu & Libchaber 1989). In §4 we report similar measurements of this oscillation frequency in our experiment. As a further characterization of this global circulation, we also measure the temperature anomaly induced in the plates versus Ra.

Takeshita *et al.* (1996) have also performed local temperature measurements near the wall, providing strong evidence that in mercury the viscous boundary layer is nested inside the thermal boundary layer, an essential difference with respect to experiments at $Pr \sim 1$.

These different studies provide a general overview of strongly turbulent Rayleigh–Bénard convection at low Pr. We examine in §5 how these results fit with the

theoretical interpretations developed for experiments at $Pr \sim 1$. In particular, the model of Shraiman & Siggia (1990) predicts that Nu increases at lower Pr (for a given Ra), while the opposite dependence is measured. We discuss how this model has to be modified at low Pr, taking into account that the viscous boundary layer is nested inside the thermal boundary layer, unlike at $Pr \sim 1$. We also stress that the different dynamics for the bulk turbulence at low and high Pr must lead to a slightly different scaling for the velocity, as detailed in Appendix A. As an alternative approach, we revisit in §5.4 the model of Castaing *et al.* (1989), and justify in §5.5 the lower Nu observed at low Pr.

2. Apparatus and experimental procedure

The cell and experimental procedure have been already described by Cioni *et al.* (1995, 1996), and a sketch of the apparatus is given in figure 1. The test chamber is a cylindrical cell with internal diameter and height equal to 21.3 cm. Both upper and bottom plates are copper, coated with nickel (50 μm thick) to avoid amalgamation with mercury. To prevent the formation of bubbles at the walls, the air in the chamber is initially pumped out, and the fluid is heated in vacuum for several hours before the tank is completely filled.

The bottom plate is heated at constant power by two Thermocoax electrical resistances, brazed to the copper with silver to ensure an excellent thermal contact. These resistances form two interlaced spirals (with a spacing of 13 mm for each), with currents in opposite directions to avoid electromagnetic effects on mercury flows. The upper plate is cooled by water circulation. A high cooling efficiency is essential: the incoming flow is divided into eight parallel pipes, injecting water in short ducts carved inside the copper plate, and leaving the plate in a symmetric way. These ducts are along concentric circles, and are designed to produce a uniform cooling. At moderate heating power (< 300 W, corresponding to $Ra < 10^8$), the temperature of the top plate is regulated by controlling the temperature of the cooling water (with a commercial thermal bath). At high power we control instead the water flow rate, using a by-pass fed by a progressive electrovalve, whose aperture is controlled by the temperature drifts at the centre of the top plate via a PID electronic circuit. The lateral wall of the cell is a thin (thickness 2 mm) stainless steel cylinder (terminated by stainless steel flanges 22 mm wide and 12 mm high to support the seals). It is thermally insulated from the outside by neoprene layers, and surrounded by a thermal screen at controlled temperature, to minimize heat losses through the lateral walls and behind the bottom plate. These losses have been measured by imposing various temperature differences between the fluid and the thermal screen. We have found a total loss coefficient of 0.2 W $°C^{-1}$. These losses are made negligible in comparison with the injected electric power (0–3 kW) by setting the top plate temperature such that the fluid is on average at the temperature of the thermal screen, and close to room temperature.

The temperature of the upper and lower plates is measured by small calibrated thermistors inserted in radial boreholes drilled into the copper plates. These temperature sensors are located at 5 cm from the cell axis and 3 mm from the plate surface in contact with the fluid. There is a small temperature drop associated with heat conduction across this 3 mm copper gap, but it is less than 1°C at the maximum power 3 kW. Temperature is also measured at the centre of the top plate (and 3 mm from the surface), and used for the thermal regulation. We study the long-time flow regime for different values of the heating power.
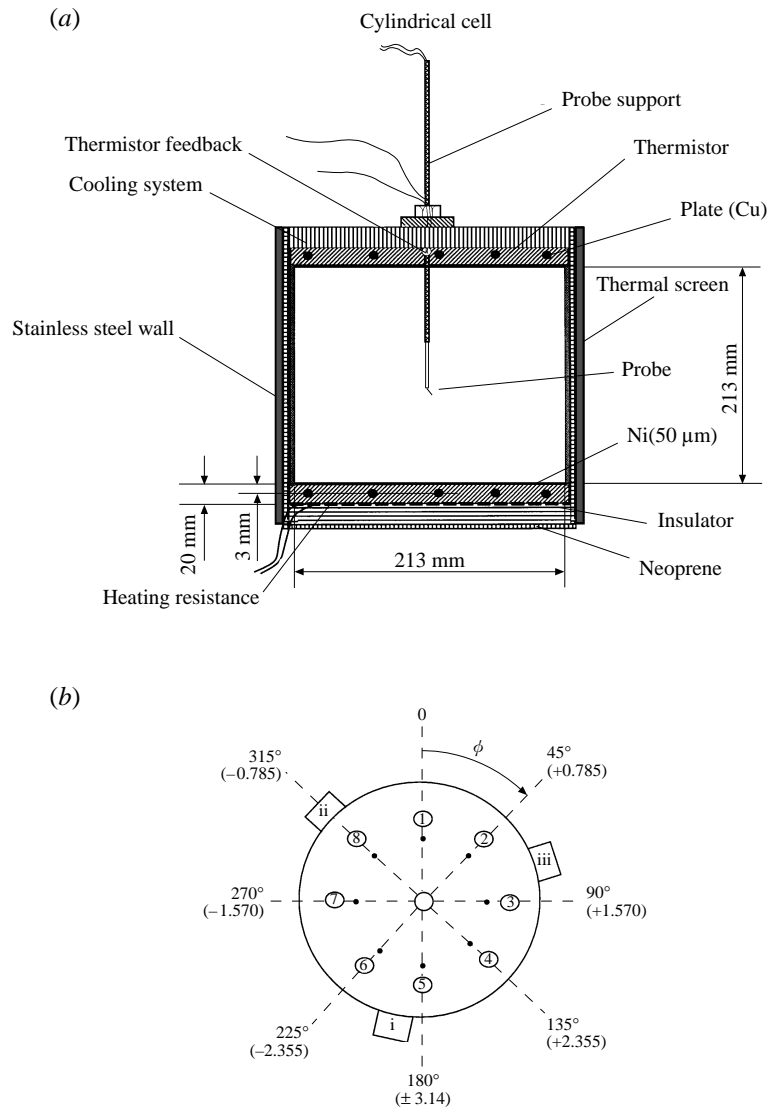
(*a*)

(*b*)

FIGURE 1. (*a*) Sketch of the experimental apparatus. (*b*) Top view showing the position of the probes (thermistors) in the bottom and top plates, with their azimuth ϕ indicated in degrees and radians. In the text, the probes are labelled by *a* for the top plate, and *b* for the bottom plate, with the subscripts given in the figure (there is also a probe inside the fluid, but the results from it are not reported in the present paper). The positions of the three feet (i), (ii), (iii) used to tilt the cell are also indicated.

The convective liquid is mercury ($0.021 < Pr < 0.026$), covering a range of Rayleigh numbers $5 \times 10^6 < Ra < 5 \times 10^9$. Experiments performed with water ($4 < Pr < 8.6$) in the same cell are also presented for comparison.

The boundary conditions require some discussion. Copper is 40 times more thermally conductive than mercury, so in the absence of convection, we can consider that the lower and upper boundaries are each at a uniform temperature. However convection greatly increases heat transfers, so that the 'effective conductivity' of mercury is increased. The analysis of Appendix B indicates that the actual boundary

condition at high Ra tends to a condition of constant heat flux at the wall (with the temperature at the centre of the top plate fixed by the regulation). The possible influence on the dynamics of this change of boundary conditions is not clear. The lateral walls are more simple: they are very thin and efficiently isolated from the outside, corresponding to a condition of no lateral flux.

3. Heat transfer measurements

3.1. *Experimental procedure*

The heat flux H^* across the convective fluid is obtained by dividing the electrical heating power by the horizontal section 356 cm². It is represented in non-dimensional form by the Nusselt number,

$$Nu = \frac{\text{total heat flux}}{\text{conductive heat flux}} = \frac{HL}{\kappa \Delta}, \tag{3.1}$$

where H is the heat flux, H^*, divided the volumic heat capacity C_F of the fluid. In order to study the dependence of Nu versus the Rayleigh number Ra (figure 2a), we determine the temperature difference, Δ, between the bottom and top plates as a function of the heating power. The value of Δ is obtained as an average over several hours because the temperature at the top and bottom fluctuates (within a few percent of Δ). Also, a systematic horizontal temperature gradient appears in each plate, due to a convective roll of the scale of the whole cell: this is the global circulation discussed in §4. Thus a spatial average over the eight probe locations in each plate is performed in order to get the mean temperature difference, Δ.

3.2. *Results with water*

The case of water has been studied first as a control. A linear regression of $\log(Nu)$ versus $\log(Ra)$ gives the following formula:

$$Nu_{H_2O} = 0.145 \, Ra^{0.292}, \quad 3.7 \times 10^8 < Ra < 7 \times 10^9. \tag{3.2}$$

The results are in excellent agreement (5% difference) with the experimental data of Chilla *et al.* (1993a), also shown in figure 2b for comparison (they give a slightly different fit $Nu \simeq 0.193 \, Ra^{0.28}$). Agreement within 5% is also obtained with Tanaka & Miyata (1980) and Chu & Goldstein (1973). The Nusselt numbers obtained by Garon & Goldstein (1973) and Goldstein & Tokuda (1980) are a little lower than ours, but still within 10%. Since these experiments used different aspect ratios and cell shapes, we confirm that these parameters have a negligible effect (less than 10%) when the aspect ratio is larger than 1 (and at sufficiently high Ra).

The fits obtained for these different experiments in water consistently give a power law $Ra^{0.285\pm0.01}$ for our range of Ra (see Goldstein, Chiang & See 1990 for a review). The same exponent is obtained for experiments in helium (Threlfall 1975; Castaing *et al.* 1989), and theoretical models justify it as a 2/7 power law (Castaing *et al.* 1989; Shraiman & Siggia 1990). Notice, however, that a slight increase of the exponent is obtained in water for $Ra > 10^{10}$ by Goldstein & Tokuda (1980). A similar increase of the exponent at $Ra > 10^{10}$ has been also observed recently in helium by Chavanne *et al.* (1996), and the exponent continuously increases up to the experimental limit $Ra = 5 \times 10^{12}$ (reaching a value ~ 0.4).
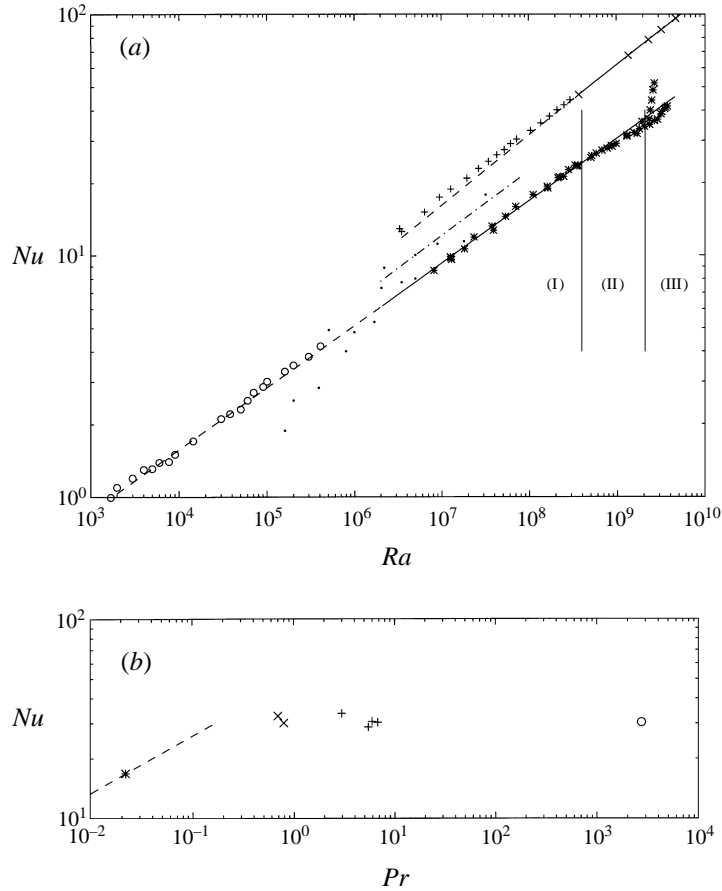
FIGURE 2. (*a*) Nusselt versus Rayleigh number for water (upper curve) and mercury (lower curves). *, Present experiments in mercury; (×), present experiments in water; +, results in water by Chilla *et al.* 1993*a*; o, results in mercury by Rossby (1969); •, results in mercury by Globe & Dropkin (1959); _ . _ ., fit of Takeshita *et al.* (1996) in mercury. The two solid lines are best fits by power laws for our experiments in water, and in mercury (region I), extended by dashed lines. (*b*) Nusselt number measured at $Ra = 1 \times 10^8$; *, our result in mercury; ×, results in gas from Fitzjarrald (1976) and Threlfall (1975); +, results in water at various mean temperatures from Chillá *et al.* (1993*a*), Tanaka & Miyata (1980), Chu & Goldstein (1973), Garon & Goldstein (1973); o, result in electro-chemical convection from Goldstein *et al.* (1990); the dashed line corresponds to the power law $Pr^{2/7}$ predicted by (5.38).

3.3. *Results with mercury*

In the case of mercury, we also observe that Nu depends on Ra as a power law close to 2/7, for $Ra < 5 \times 10^8$. A transition with an increased heat transfer is suggested at $Ra = 2 \times 10^9$. This contrasts with the progressive increase observed in water and helium. Furthermore this increase is preceded by a slight decrease of the exponent.

More precisely we distinguish three different ranges, where the least-square fits give the following results.

(i) Region I of figure 2(*a*), ranging from $Ra = 7.0 \times 10^6$ to $Ra = 4.5 \times 10^8$ obeys the scaling law

$$Nu_{HgI} = (0.140 \pm 0.005)\, Ra^{(0.26 \pm 0.02)}. \tag{3.3}$$

This law also provides an excellent fit to the results of Rossby (1969) ($Nu \simeq 0.147Ra^{0.257}$), suggesting that it holds in the whole range $2 \times 10^4 < Ra < 4.5 \times 10^8$. The exponent is in agreement with the fit $Nu \simeq 0.155\ Ra^{0.27}$ obtained by Takeshita *et al.* (1996), but the values of Nu are a little lower in our experiments, as shown in figure 2(a) (although the two experiments have the same cylindrical geometry and the same aspect ratio 1). There is also a reasonable agreement with the old data of Globe & Dropkin (1959), also shown in figure 2(a), but these are strongly scattered and do not provide a reliable fit.

(ii) Region II, ranging from $Ra = 4.5 \times 10^8$ to $Ra = 2.1 \times 10^9$, scales as

$$Nu_{HgII} = (0.44 \pm 0.015)Ra^{(0.20 \pm 0.02)}. \tag{3.4}$$

(iii) Finally, for Rayleigh numbers larger than $Ra \simeq 2.1 \times 10^9$ a sharp increase of Nu is observed (region III of figure 2a). This transition is difficult to study as it is obtained near the maximum Ra that we can reach with our apparatus. Furthermore, we have observed drifts of the Nusselt number: two extreme behaviours are indicated (by stars) in figure 2(a). This contrasts with the excellent reproducibility in regions I and II (including the slope decrease in region II). The transition effect in region III is quite significant: it corresponds in practice to a decrease of Δ by 20 °C (20% of Δ) for a given heating power, and could not be explained by any experimental flaw. The transition is possibly related to the onset of some instability occurring in the viscous boundary layer, as discussed in §5.3. Such boundary layer instabilities are known to be very sensitive to the state of the surface of the wall, which could explain the lack of reproducibility (due to ageing of the wall in contact with mercury).

3.4. *Discussion of the Prandtl number dependence*

The comparison of heat transfers in water and mercury clearly establishes that Nu is smaller for smaller Pr, at a given Rayleigh number. For instance, at $Ra = 10^9$, $Nu = 30$ in mercury, half that for water, in agreement with similar comparisons made by Globe & Dropkin (1959), Rossby (1969), and Kek & Muller (1993) at lower Ra.

By contrast, different experiments made for Pr equal to or higher than 0.7 indicate a constant Nu within better than 10%. We have represented in figure 2(b) this dependence on Prandtl number for a given $Ra(= 10^8)$. The results for water ($Pr \sim 6$) and air ($Pr \sim 0.7$) are the same within the experimental errors, as are the results† in helium ($Pr = 0.8$) by Threlfall (1975). Recent numerical computations confirm that Nu is independent of Pr for $Pr \sim 1$ (R. Tripiccione, private communication). The result for electrochemical convection by Goldstein *et al.* (1990), equivalent to thermoconvection at $Pr \sim 2700$, is also the same. The much lower Nu obtained in mercury, therefore, clearly contrasts with results at moderate and high Pr.

This dependence on Pr agrees with the theory of Kraichnan (1962), which predicts $Nu \sim Pr^{1/3}$ for $Pr < 0.1$ and constant for $Pr > 0.1$ (with a $Ra^{1/3}$ law in both cases). It contradicts the $Pr^{-1/7}$ law predicted by Shraiman & Siggia (1990): the sign of variation in Pr is opposite. The same dependence in $Pr^{-1/7}$ would also result from the mixing zone model of Castaing *et al.* (1989). The later theories, however, successfully predict the Ra dependence, and we propose in §5 adaptations to account

† The Nusselt number obtained by Castaing *et al.* (1989) at $Ra = 10^8$ is about 20% higher, and the comparison with water would therefore indicate a significant decrease with Pr. However this experiment was not optimized for absolute measurements of heat flux (but rather designed to cover a very wide range of Ra). New measurements by Chavanne *et al.* (1996) suggest that the Nusselt number obtained by Castaing *et al.* (1989) for $Ra \sim 10^8$ was too high. These new measurements are very close to results in water, confirming the very weak dependence on Pr.

for the observed behaviour at low Pr. However, the various experimental results cannot be fitted with simple power laws in a wide range of Ra and Pr. Notice also that the exponent in Ra seems to increase with increasing Pr (0.26 in mercury, 0.28–0.29 for $Pr \sim 1$, 0.33 obtained for high Pr by Goldstein *et al.* 1990), so the problem is quite complex.

4. Properties of the global circulation

4.1. *Characterization of the global circulation*

The spontaneous formation of a mean flow, in a cell with large aspect ratio, was described by Krishnamurti & Howard (1981)†. It is characterized by a systematic drift of the plumes, appearing for $Ra > 2.5 \times 10^6$, and is therefore quite distinct from the rolls produced near the instability threshold. A global circulation has been also noticed in experiments at higher Ra (but in a more confined geometry, with aspect ratio of order 1). It has been detected in helium by temperature correlations between two probes (Sano *et al.* 1989), and visualized and measured in water at $Ra \simeq 10^9$ by Tilgner, Belmont & Libchaber (1993). Cioni *et al.* (1996) and Takeshita *et al.* (1996) have shown that such a global circulation also forms in mercury, persisting in the whole explored range $10^6 < Ra < 5 \times 10^9$.

The presence of the global circulation is indirectly detected in our experiments by the dipolar temperature distribution induced along the bottom and top plates. As shown schematically in figure 3, the side of the top plate receiving the rising flow is expected to be warmer than average, and the opposite side cooler. On this cooler side, the bottom plate receives a downward flow and is therefore also expected to be cooler than average. Such a dipolar temperature structure forms spontaneously along both plates (see figure 3). It is detected with the eight probes (thermistors) inside the bottom and top plates respectively (their positions are sketched in figure 1*b*). The temperature at the centre of the top plate, used for the thermal regulation, always corresponds to the average over the eight peripherical probes. This dipolar structure can be characterized by an amplitude Δ_h and an azimuthal angle. Cioni *et al.* (1996) found that a slight tilt of the cell directs the dipolar structure in the expected direction: i.e. the flow follows the azimuth of maximum rising slope along the bottom plate. The strength of the global circulation, characterized by the amplitude Δ_h, is practically independent of this tilt angle, showing that the global circulation is spontaneously formed. It is not due to a small tilt, or other experimental defect, but it is oriented by it.

4.2. *Dynamics of the global circulation*

When the cell is horizontal, the azimuth of the global circulation slowly changes with time, resulting in fluctuations on long time scales of the temperature at the periphery of each horizontal plate. An example of a four-day record of the bottom plate is shown in figure 4, showing random jumps between two average values. Simultaneous jumps of opposite direction occur on the other side of the bottom plate, while the temperature at the centre of the plate remains at the average value (see figure 5 of Cioni *et al.* 1996). The same jumps occur on the top plate, so that the vertical temperature difference at a given azimuth is not modified. All these observations indicate that the jumps correspond to reversals of the global circulation azimuth.

† Velocity has been measured in earlier experiments, e.g. by Garon & Goldstein (1973), but the study focused on fluctuations and did not mention a global circulation.
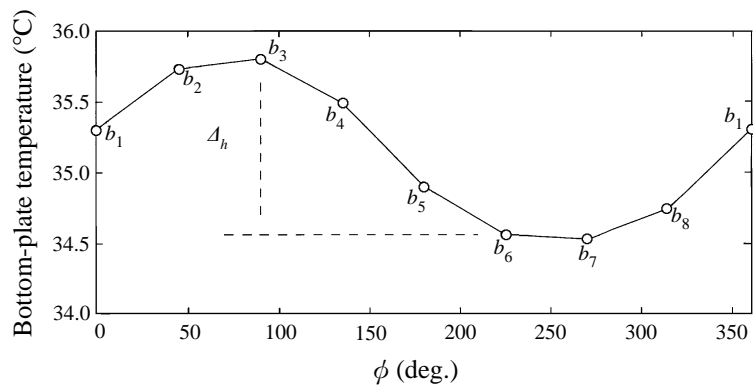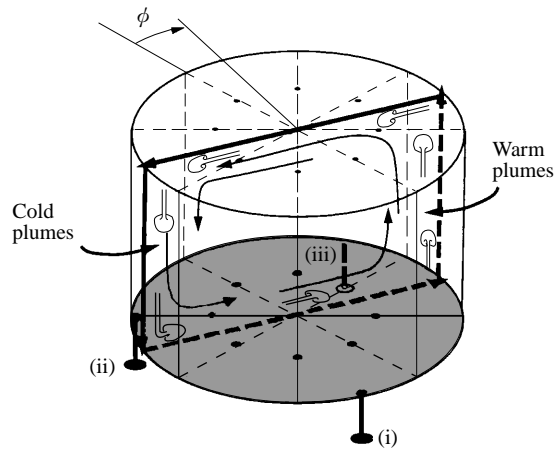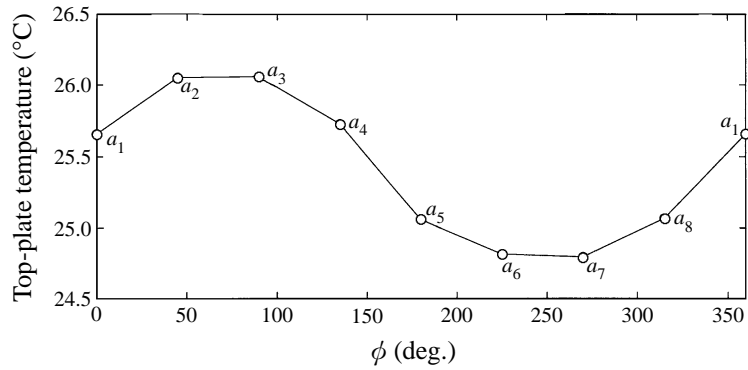
FIGURE 3. Spatial structure of the global circulation in mercury ($Ra = 3.5 \times 10^8$), sketched in the centre figure, and detected by the plot of temperature versus azimuthal angle ϕ along the top and bottom plates. The global circulation azimuth is fixed by raising one of the three feet (i), (ii), (iii) of the cell, producing a tilt angle of $0.5°$ (the temperature is averaged over 5 min.). The crest-to-crest temperature is denoted Δ_h.
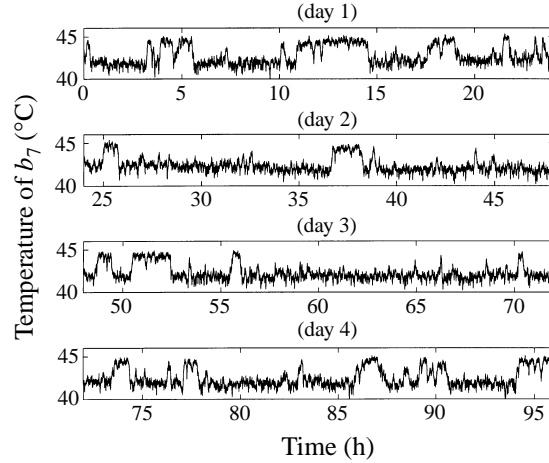
FIGURE 4. Typical time signal of a thermistor (b_7) in the bottom plate at $Ra = 8.7 \times 10^8$. Note the random reversals occurring with typical time intervals of several hours.

The global circulation never disappears, maintaining its strength as it changes in azimuth. This is illustrated by the successive azimuthal temperature profiles during a reversal, shown in figure 5: the position of the temperature maximum shifts by 180°, while the amplitude Δ_h does not significantly change. This observation is checked in a more systematic way by computing at each time t the azimuthal Fourier transform of the temperatures $b_i(t)$. We thus obtain the phase Φ and amplitude $|M|$ of the dipolar mode from the first Fourier components A_1 and B_1 given by

$$
\left.
\begin{aligned}
A_1(t) &= \frac{1}{2}\sum_{i=1}^{8} b_i(t)\cos\phi_i, \quad B_1(t) = \frac{1}{2}\sum_{i=1}^{8} b_i(t)\sin\phi_i, \\
M(t)^2 &= A_1^2 + B_1^2, \quad \Phi(t) = \mathrm{sign}(B_1)\,\arccos\frac{A_1}{|M|}.
\end{aligned}
\right\}
\tag{4.1}
$$

(The coefficient $1/2$ is introduced so that M coincides with Δ_h for a pure dipolar mode.) The time records of figure 6, spanning two days, indicate that the amplitude fluctuates around a mean value but never vanishes. Jumps in the temperature are due to 180° phase shifts. Probability distribution functions of the temperature at a given probe (b_7) have two peaks (between which the jumps occur). The p.d.f. for the phase indicates a strong minimum around $\phi \sim \pi$ (or $-\pi$), so the azimuth remains roughly in the same half-space during reversals. We notice that the p.d.f. of ϕ is broadly distributed in this half-space, corresponding to the occurrence of phase drifts as well as complete reversals.

This dynamics of reversals and phase drifts is probably sensitive to small defects of the experimental system. To control the system, we tilt the cell slightly (angle 0.5°), lowering foot (iii) located at $\phi = 75°$ (see figure 1b), which produces a maximum temperature at the opposite azimuth $\phi \simeq 255°$. The signal at probe b_7 close to this location is shown in figure 7(a), showing that the reversals are suppressed. This suppression is confirmed by the phase record in figure 7(c) (compare with figure 6c). The phase is set to a mean value $\Phi = -1.61\,\mathrm{rad} = 268°$, close to the value 255° expected from the tilt direction. Significant phase fluctuations remain, with r.m.s. 0.42 rad, but much lower than when reversals occur. By contrast the mean amplitude $\overline{M}=$
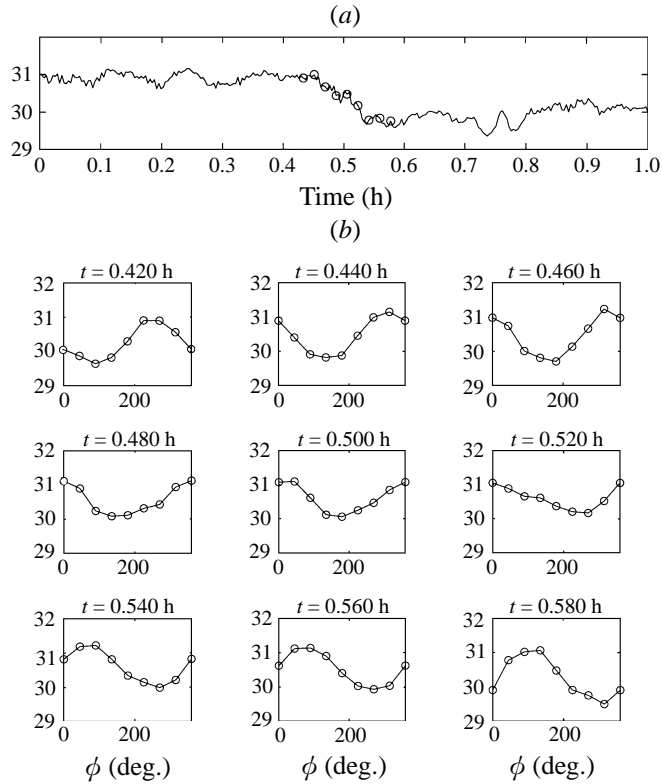
FIGURE 5. (*a*) Time signal of thermistor b_7 showing a single reversal (detail of the first hour of the time series in figure 6*a*), at $Ra = 3.5 \times 10^8$. (*b*) Successive azimuthal temperature profiles during the reversal, at times indicated by the circles in (*a*): the dipolar structure shifts in azimuth, keeping a constant amplitude, corresponding to a global rotation of the global circulation azimuth.

1.46 °C remains nearly the same as without tilt ($\overline{M} = 1.40$ °C), and the r.m.s. 0.24 °C is unchanged.

It is remarkable that most of the fluctuations measured in the plates correspond to these fluctuations of phase and (to a lesser extent) amplitude in the global circulation, as indicated by the cross-correlations between the signals of the different probes. In figure 8(*a*), we represent these cross-correlations for the probes in the bottom plate with respect to a reference probe (b_5), also in the bottom plate. The purely spatial cross-correlations (with time delay zero) are represented vs. azimuth in the central graph. The strong negative cross-correlation (-0.7) with the opposite probe (b_1) indicates that at least 70% of the fluctuations are dipolar. Imperfections of the temperature regulation system would result in fluctuations *positively* correlated at all locations, and random noise would lead to uncorrelated fluctuations. The changes of the global circulation are therefore *intrinsic* fluctuations, due to some chaotic dynamics. The cross-correlations with time delay are represented in the outer plots for the different probes. They indicate that the temperature fluctuations remain spatially coherent over a correlation time of about 200 s, which can be interpreted as a typical time for changes of the global circulation. It is about 10 times the convective circulation time L/U, in agreement with the time necessary for a reversal (see figure 6). Similar results are obtained in figure 8(*b*) when the reference probe is on the top
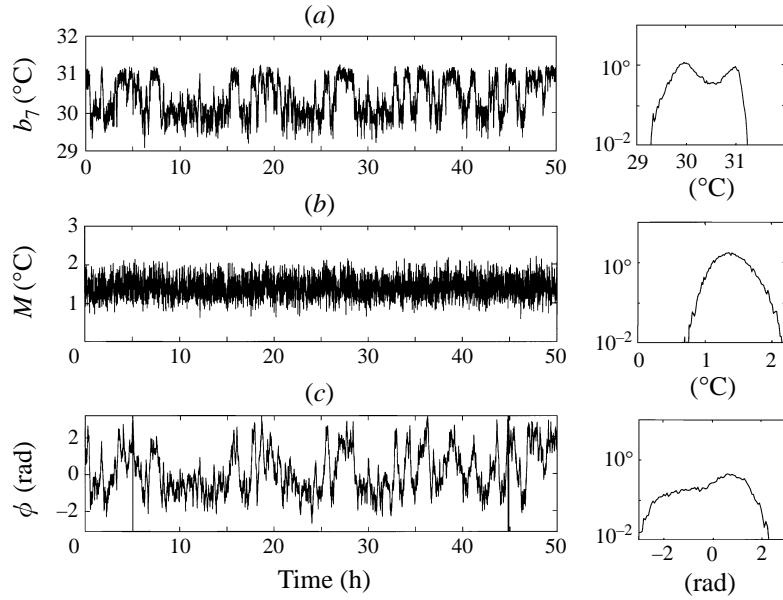
FIGURE 6. Amplitude and phase of the dipolar structure ($Ra = 3.5 \times 10^8$). Time series (over 50 hours) on the left, and the corresponding probability distribution functions (with logarithmic ordinate) on the right. (*a*) Temperature at thermistor b_7, showing reversals. (*b*) Amplitude M, defined by (4.1). The mean value is 1.40 °C with an r.m.s. 0.24 °C. (*c*) Azimuth Φ (in radians). The r.m.s. of Φ is 1.18 rad, around a mean value 0.02 rad.
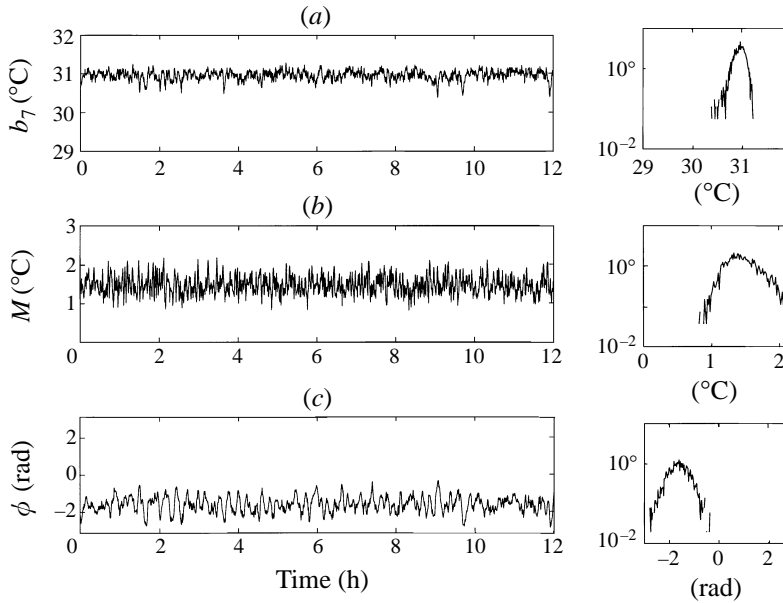
FIGURE 7. Same as figure 6, but with a small tilt 0.5° of the cell, obtained by lowering foot (iii) (see figure 1*b*) (the recording time is 12 hours). The probe signal b_7 in (*a*) indicates that reversals are suppressed. The mean amplitude M (1.46 °C) is nearly unchanged by the tilt as is the r.m.s. amplitude (0.24). In contrast, the azimuth is set to $\overline{\Phi} = -1.61$ rad by the tilt, and the r.m.s. of Φ is reduced to 0.42 rad.
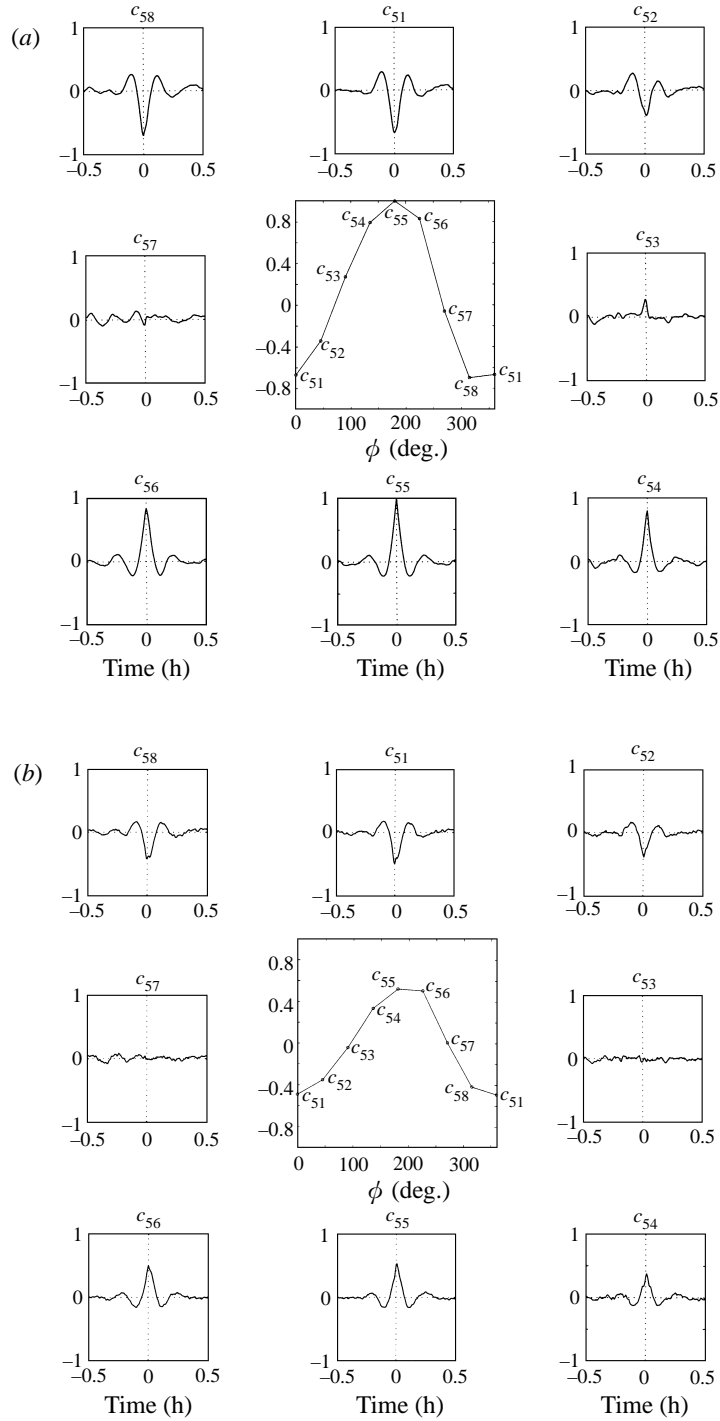
FIGURE 8. Cross-correlations, (*a*) Between a reference probe b_5 and the other probes b_j in the bottom plate (same conditions as figure 7). The cross-correlations are plotted versus time delay at the periphery, and the value with zero time delay is represented versus azimuth ϕ in the central plot. (*b*) Between a reference probe a_5 in the top plate, and the probes in the bottom.
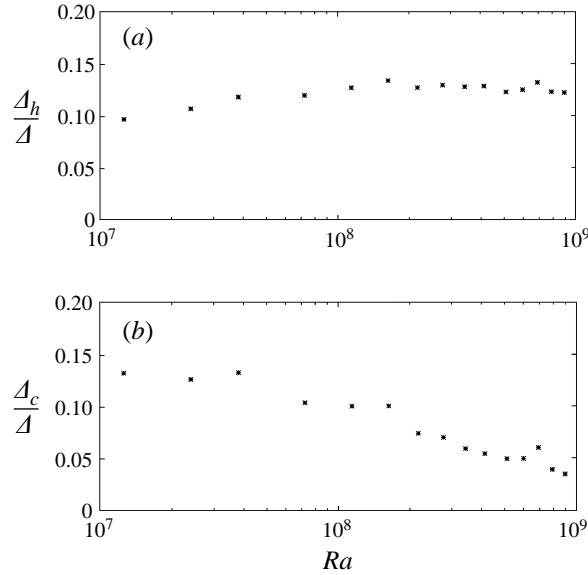
FIGURE 9. Horizontal temperature difference Δ_h in the bottom plate: (*a*) Δ_h/Δ versus *Ra*;
(*b*) Corrected temperature Δ_c/Δ, estimated in the bulk by (B 12) derived in Appendix B.

plate, confirming the similarity of the dipolar structure on the top and bottom plates, even during fluctuations.

In summary, the global circulation forms spontaneously and is quite robust and well defined; its amplitude fluctuates, with a time scale of several minutes, but never vanishes (figure 6*b*). It also fluctuates in azimuth, and this azimuthal motion can be confined by a small tilt of the cell (e.g. by 0.5°), while the amplitude is not modified by the tilt. When the cell is horizontal, we would expect that the azimuth uniformly wanders due to the axisymmetric geometry. In reality our system preferentially stays in a half-space, clearly set by small defects of our system, probably a slight inhomogeneity of heating ($< 1\%$).

4.3. *Scaling of Δ_h with Ra*

To study the scaling of the global circulation with *Ra*, we impose a small tilt (0.5°), which avoids reversals of the global circulation, but does not change the amplitude Δ_h. We have also checked that the heat transfer is unchanged (by no more than 1% even for a much higher tilt of 4°), confirming that this tilt has a negligible influence on the dynamics, except for maintaining a constant direction global circulation.

The horizontal temperature difference, normalized by Δ, is plotted in figure 9(*a*) versus *Ra*. This ratio Δ_h/Δ is nearly constant. The relation between Δ_h and the convection dynamics is unfortunately not straightforward. The simplest hypothesis is to assimilate Δ_h into a typical horizontal temperature difference in the bulk, called Δ_c in §5.1. However, the heat conduction in the copper plate tends to filter out the dipolar structure in a way depending on *Nu*, as discussed in Appendix B. Another effect is taken into account in Appendix B: the thermal boundary layer grows along the plate following the global circulation, so that the heat transfer is more efficient on the side of incoming global circulation (with a thinner boundary layer). The ratio Δ_c/Δ for the bulk obtained after correcting for these effects, using (B 12) of Appendix B, is plotted in figure 9(*b*).
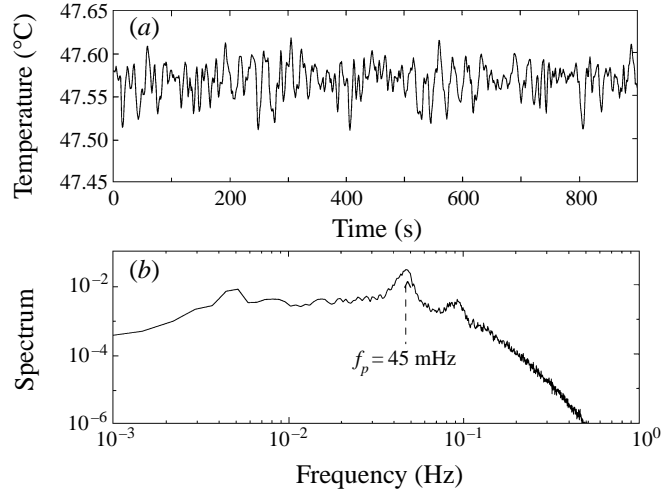
FIGURE 10. (*a*) Typical signal of one thermistor (b_7) in the bottom plate as a function of time. The azimuthal angle corresponds to a maximum temperature, $Ra = 8.7 \times 10^8$; (*b*) the corresponding power spectrum, showing the peak at the characteristic frequency f_p. This peak corresponds to the circulation frequency of the large-scale flow inside the cell.

Δ_c/Δ slowly decreases with increasing Ra. The theoretical prediction (5.40) leads to $\Delta_c/\Delta \sim Ra^{-1/7}$. A prediction of $Ra^{-1/5}$ will be given in §5.3, equation (5.24), for region II. Our experimental results are compatible with these predictions. However our estimate of Δ_c/Δ is indirect, using the theoretical relation (B 12) of Appendix B.

4.4. *Velocity in the global circulation deduced from an oscillation frequency*

Another characterization of the global circulation is provided by a temperature oscillation occurring near the bottom and top plates, observed in helium by Castaing *et al.* (1989) (but wrongly interpreted as an oscillation of a stably stratified bulk). It was later interpreted by Sano *et al.* (1989) as a boundary layer instability 'transported' along the cell by the global circulation. The oscillation is in quadrature at each corner, and the oscillation frequency, f_p, corresponds to transport by the maximum velocity U of the global circulation, $f_p \simeq U/(4L)$ (U is a vertical velocity measured along a sidewall). This oscillation was observed in the whole range of Ra investigated ($10^8 < Ra < 10^{11}$), see figure 14 of Sano *et al.* (1989). In non-dimensional form, defining $\omega_p = 2\pi f_p$, and $Re = UL/\nu$, we write

$$\frac{\omega_p L^2}{\kappa} = \tfrac{1}{2}\pi \, Re Pr. \qquad (4.2)$$

Some assertions involving the thermal boundary layer instability are given by Sano *et al.* (1989) to explain the mechanism of the oscillation. This interpretation has been made more precise by Villermeaux (1995), who proposed a dynamical model of two unstable modes, in the bottom and top boundary layers, coupled with a delay corresponding to transport by the velocity U. The nonlinear saturation of the instability occurs after this delay, and leads to a spontaneous oscillation. The resulting frequency is close to (4.2).

Takeshita *et al.* (1996) have detected the same oscillation in mercury. They have checked that its frequency is proportional to the global circulation velocity, measured from the correlations between two temperature probes (they propose relation (4.2), but with a prefactor 2 instead of $\pi/2$). We have observed the same oscillation from
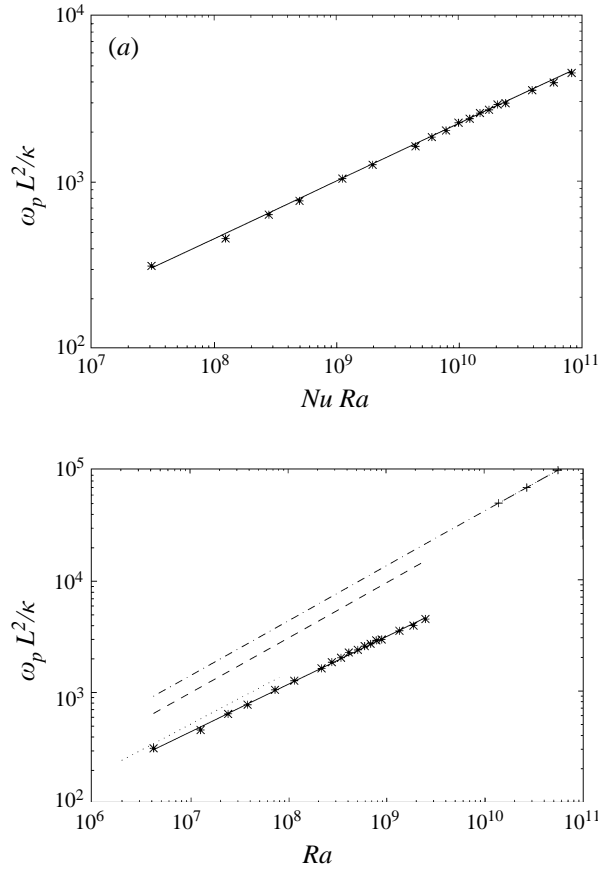
FIGURE 11. The dependence of the characteristic frequency ω_p, normalized by κ/L^2: (*a*) versus the non-dimensional power *NuRa*, with the best fit (4.3); (*b*) versus *Ra*, with the best fit (4.4) (solid line), compared with the fits of Takeshita *et al.* (1996) (dotted line), of Castaing *et al.* (1989) in helium (dashed line); results in water are indicated by (+) and fitted and extrapolated by the dot-dashed line (note that the geometry of this experiment by Ciliberto *et al.* 1996 is different: a box with square vertical section of 40×40 cm and relatively narrow width 10 cm).

temperature measurements in the plates. A typical signal is shown in figure 10(*a*), and the corresponding Fourier spectrum in figure 10(*b*). An oscillation period is clearly identified, although it is superposed on a significant amount of turbulent noise†. We have measured similar signals at different probes at the top and bottom, and it appears that the oscillation is only detected where the temperature is extremal (here at azimuth $\sim 90°$ and $\sim 270°$). The oscillation is not observed where the temperature is close to average (at azimuth $\sim 180°$ and $\sim 0°$), but rather occurs at positions with a strong global circulation, as sketched in figure 3. We also observe that the oscillation is in quadrature between the two sides and between the top and bottom at the same azimuth. These phase shifts reveal a direction of rotation, which agrees with transport by the flow. The phase shift reverses when we reverse the tilt. The frequency does not depend on the tilt angle.

† This oscillation is quite distinct from the fluctuations discussed in §4.2: the time scale is much shorter, 20 s instead of 200 s or more for reversals, and the amplitude is smaller by more than an order of magnitude. The pattern of spatial cross-correlations is different.

The frequency ω_p, normalized by κ/L^2, is plotted in figure 11(a) versus the non-dimensional heating power $NuRa$. The best fit gives

$$\frac{\omega_p L^2}{\kappa} = 0.81\,(NuRa)^{0.343}, \tag{4.3}$$

in excellent agreement with the exponent 1/3 predicted for a free fall velocity (see (5.6)). The fit is again limited to region I, but no significant change is observed in region II. Introducing the relation Nu vs. Ra in the fit (4.3), we then expect that $\omega_p \sim Ra^{0.43}$ in region I, $\omega_p \sim Ra^{0.41}$ in region II. The representation of ω_p versus Ra is shown in figure 11(b) but the two regimes cannot be really distinguished at our experimental precision. A fit

$$\frac{\omega_p L^2}{\kappa} = 0.470\,Ra^{0.424} \tag{4.4}$$

is obtained. Assuming (4.2), we can deduce

$$Re = 12.0\,Ra^{0.424}. \tag{4.5}$$

Our result (4.4) is in reasonable agreement with the fit $\omega_p L^2/\kappa = 0.31\,Ra^{0.46\pm0.02}$ obtained by Takeshita *et al.* (1996), and also shown in figure 11(b).

Castaing *et al.*'s (1989) results in helium show larger values at a given Pr as expected. The exponent of Ra in helium disagrees somewhat with the prediction (5.17) derived in the next section. The ratio of the result in helium to our result ranges from 2.0 to 3.0 for $5 \times 10^6 < Ra < 10^9$. In §5, we give theoretical predictions of the dependence on Pr, equations (5.39), for $Pr < 0.3$ and (5.17) for $Pr > 0.3$. A ratio of 3.5 between helium and mercury is predicted from these two relations, in the right direction and range, but not very precise due to the difference in power law with Ra. We have observed the same oscillation in water, and the non-dimensional frequency is greater than the frequency in helium, as expected. However we did not investigate this problem systematically in water with the same apparatus, but plot in figure 11(b) results from another experiment, by Ciliberto, Cioni & Laroche (1996).

5. Discussion of theoretical predictions

5.1. *Scaling in the bulk*

All theories of turbulent thermal convection distinguish clearly two regions. In the bulk, the turbulent mixing is efficient and consequently the mean temperature gradient is weak. The temperature gradients, expelled from the bulk, are confined to diffusive boundary layers near the bottom and top walls.

The thickness λ of the diffusive boundary layer is obtained from the exact relation $H = -\kappa(\partial T/\partial z)_{z=0}$, corresponding to the scaling (using definition (3.1))

$$\lambda/L = 0.5\,Nu^{-1} \tag{5.1}$$

(the coefficient 0.5 indicates that half of the temperature drop is across each boundary layer).

In the bulk, temperature is transported by the correlation $w\theta$ (of the vertical velocity component w and temperature fluctuations θ). This quantity scales as $U\Delta_c$ (where U is a typical velocity and Δ_c a typical temperature fluctuation in the bulk), so that we expect the heat flux H (defined in §3.1) to scale like

$$H \sim U\Delta_c. \tag{5.2}$$

The free fall relation is also assumed in the bulk,

$$U \sim (\alpha g L \Delta_c)^{1/2}. \tag{5.3}$$

The combination of (5.2) and (5.3) yields Δ_c and U as a function of the heat flux. It is convenient to express these quantities in non-dimensional form, as Δ_c/Δ and

$$Re = \frac{UL}{\nu}. \tag{5.4}$$

Then, using the definitions (1.1), (1.2), (3.1), we get

$$\Delta_c/\Delta \sim Nu^{2/3} Ra^{-1/3} Pr^{-1/3}, \tag{5.5}$$

$$Re = A (NuRa)^{1/3} Pr^{-2/3}, \quad \text{with} \quad A \simeq 2.0, \tag{5.6}$$

where the value of A is a fit to our results, obtained by combining (4.2) and (4.3).

The free fall relation (5.6) can be also obtained by alternative assumptions (without using (5.2) and (5.3)), starting from the exact relation expressing the energy budget in the Boussinesq equation:

$$(Nu - 1)Ra = \langle |\nabla u|^2 \rangle L^4/\kappa^2. \tag{5.7}$$

Physically, the convective heat flux $\overline{w\theta}$ transports a flux of potential energy $\alpha g z \, \overline{w\theta}$ (each fluid particle has a potential energy $\alpha g z \theta$). The divergence of this flux is just $\alpha g \overline{w\theta}$ and in a steady regime, it must be locally balanced by the viscous energy dissipation $\nu|\nabla u|^2$. Equation (5.7) expresses this balance, averaged over the whole domain. If we assume ordinary fully developed turbulence in the bulk, the energy dissipation $\nu|\nabla u|^2$ is controlled by advective effects and scales like U^3/L. Introducing this scaling in (5.7) yields (5.6).

We have seen in §4.4 that this scaling law is in excellent agreement with our experiments in mercury. By contrast a significant discrepancy has been observed in helium by Sano *et al.* (1989). Shraiman & Siggia (1990) interpret this discrepancy by assuming that kinetic energy dissipation occurs mostly in turbulent boundary layers, described by the classical logarithmic law. Energy dissipation then basically scales like U^3/L, but with a logarithmic correction, providing a better fit to the experiments in helium, as shown in figure 5 of Siggia (1994). However, the issue is not clear, as the boundary layer over a flat plate supposedly becomes turbulent and satisfies the logarithmic law only for $Re > 3 \times 10^5$ (see e.g. Schlichting 1968, p. 600). This value is only reached at $Ra \sim 10^{12}$ in helium, close to the upper limit of the experiments. The Reynolds number is even lower in water (10^3 at $Ra = 10^9$), as stressed by Tilgner *et al.* (1993). Therefore significant energy dissipation could occur in the bulk. The different exponent for Re vs. Ra in helium and mercury could be related instead to the different turbulence dynamics revealed by temperature time spectra, as discussed in Appendix A.

In spite of this small discrepancy for the exponent of Ra, (5.6) provides a convenient estimation of the maximum global circulation velocity, U, measured in various experiments (either along the horizontal or the vertical walls). The prefactor A was fitted for our experiments with mercury; it yields for instance $Re = 3 \times 10^4$ for $Ra = 10^8$. In helium (5.6) predicts, using measured relation Nu vs. Ra, for $Ra = 10^{10}$ a value $Re \simeq 2.6 \times 10^4$, close to the value 2×10^4 obtained by Sano *et al.* (1989), from measurements of the vertical velocity near a sidewall. The prediction for water at $Ra = 10^9$ is $Re \simeq 1000$, while the experimental value of Tilgner *et al.* (1993) is 1400. However, the latter corresponds to the maximum horizontal velocity near the top

wall, while the vertical velocity was measured in helium, and the similarity between these two components remains to be checked.

The velocity profile near the top wall was directly measured by Tilgner *et al.* (1993): the global circulation is a parietal jet with a maximum velocity at a distance δ from the wall of roughly

$$\delta/L \simeq 0.04. \tag{5.8}$$

This ratio is also obtained in a gas by Belmonte, Tilgner & Libchaber (1994), remaining constant in the range of $10^7 < Ra < 10^{10}$. Takeshita *et al.* (1996) find a result close to (5.8) in mercury by the same procedure. Notice however that this velocity is not directly measured, but deduced from the maximum frequency excited above the noise level in the temperature spectra, which is a questionable method. A simple interpretation of (5.8) is that it corresponds to the classical result that a turbulent jet spreads with a constant angle.

The shear $\gamma = (\partial u/\partial z)_{z=0}$ at the wall has been estimated by Shraiman & Siggia (1990), assuming that the boundary layer is turbulent with the classical logarithmic velocity profile:

$$u(z) = u_* \, [2.5 \ln(u_* z/v) + 5], \tag{5.9}$$

where u_*^2 is the turbulent stress, constant across the layer. Matching to the velocity U measured at the distance $\delta = 0.04 \, L$ from the wall leads to

$$(u_*/U) \, [2.5 \ln(Re \, u_*/U) - 3] = 1. \tag{5.10}$$

For a typical $Re \sim 10^4$, (5.10) yields $u_*/U \sim 0.07$. The matching of the turbulent stress u_*^2 to the viscous stress at the wall yields $v\gamma = u_*^2$, so that

$$\gamma \simeq 0.005 \, U^2/v. \tag{5.11}$$

Defining the thickness λ_v of the viscous boundary layer by $\gamma\lambda_v = U$, (5.11) is equivalent to

$$\lambda_v/L \simeq 140/Re. \tag{5.12}$$

Notice that the thickness λ_v of the viscous sublayer differs from the position of the velocity maximum δ, representing the thickness of the turbulent boundary layer.

Tilgner *et al.* (1993) have directly measured λ_v and find $\lambda_v/L = 0.02$ for $Re \sim 1400$ (at $Ra = 10^9$ in water). In that case, λ_v is close to δ (but the ratio of these lengths must increase with increasing Re, as indicated by (5.12) and (5.8)). In the case of Tilgner *et al.* (1993), (5.12) leads to $\lambda_v/L = 0.1$, and including the logarithmic correction of (5.9) would lead to $\lambda_v/L = 0.06$, still three times thicker than the measurement of Tilgner *et al.* (1993). Shraiman & Siggia (1990), using a different constant in (5.9) would find a result still 3 times thicker than ours. Therefore the estimation of the wall shear must be considered with caution, especially for $Pr > 1$ and moderate Ra: this derivation involves only shear-driven turbulence, while buoyancy-driven turbulence is also important in the observed Bolgiano–Oboukhov dynamics (see Appendix A). The validity of (5.9) is probably better justified for low Pr, when turbulence has a Kolmogorov dynamics.

5.2. *The thermal boundary layer and the relation Nu vs. Ra for Pr $\sim$ 1*

Complete predictions must relate Nu, or equivalently λ, to Ra. Shraiman & Siggia (1990) obtained the 2/7 power law for Nu vs. Ra by assuming that the thermal boundary layer is nested inside the viscous subrange, which is justified for $Pr \sim 1$ as discussed below. In their view, the only effect of buoyancy is to globally drive the

global circulation, and temperature in the boundary layer is just passively transported by this global circulation. Furthermore the thermal boundary layer is assumed to develop with a velocity $u = \gamma z$ with constant shear γ. Its thickness λ then varies as $(L\kappa\gamma^{-1})^{1/3}$. (This can be understood physically by considering that the boundary layer grows with time t in $(\kappa t)^{1/2}$, following fluid particles, and the distance travelled is $x \sim \gamma\lambda t$.) The corresponding temperature profile has been analytically determined by Shraiman & Siggia (1990), and found in good agreement with experiments in water by Chilla *et al.* (1993*a*), and with the numerical computations of Bartoloni *et al.* (1993) and Kerr (1996). The solution yields a local heat flux:

$$H = -\kappa\frac{\partial T}{\partial z} = 0.269\ \Delta\ (\kappa^2\gamma/L)^{1/3}\ (x/L)^{-1/3}, \tag{5.13}$$

where x is the distance travelled along the boundary layer. Introducing the shear (5.11) in this relation we get (averaging the flux from 0 to x)

$$Nu_{(Pr\sim1)} = 0.07\ Re^{2/3}\ Pr^{1/3}\ (x/L)^{-1/3}. \tag{5.14}$$

Combining (5.14) with (5.6) yields

$$Nu_{(Pr\sim1)} = 0.16\ Ra^{2/7}\ Pr^{-1/7}. \tag{5.15}$$

We have assumed $x/L = 0.1$, to fit the prefactor in (5.15) with experiments at $Pr \sim 1$. The estimates (5.5) and (5.6) are then completely specified:

$$(\Delta_c/\Delta)_{Pr\sim1} \sim Ra^{-1/7}Pr^{-3/7}, \tag{5.16}$$

$$Re_{Pr\sim1} = 1.1\ Ra^{3/7}Pr^{-5/7}. \tag{5.17}$$

Note that these results are sensitive to the distance x/L (Nu would vary as $(x/L)^{-3/7}$). It can be expected that x is the distance travelled between plumes rather than L, and the ratio $x/L \sim 1/10$ may correspond to a triggering of the plumes by the large eddies of the jet, which typically scale like $L/10$. Many assumptions have been introduced to get (5.15), but interestingly the same scaling is obtained by the model of Castaing *et al.* (1989), which does not depend on the presence of a well-organized bulk flow. We reproduce this model in §5.4, and extend it to the case of low Pr in §5.5.

The derivation of (5.15) is valid as long as the thermal boundary layer is nested inside the viscous sublayer. Estimating the latter by (5.12) and the former by (5.1), we get

$$\lambda/\lambda_v = 0.004\ Re/Nu. \tag{5.18}$$

Expressing Re and Nu by (5.6) and (5.15), this yields

$$\lambda/\lambda_v = 0.02\ Ra^{1/7}\ Pr^{-4/7}. \tag{5.19}$$

The condition $\lambda/\lambda_v < 1$ is then satisfied when

$$Ra\ <\ 10^{12}\ Pr^4. \tag{5.20}$$

This estimate has the same form as the one given by Shraiman & Siggia (1990), with a slightly different prefactor. The Pr^4 dependence is only weakly modified if we assume that Nu is independent of Pr (as suggested by experiments) instead of varying as $Pr^{-1/7}$.

What is expected beyond this threshold depends on the Prandtl number. For

$Pr \sim 1$, we expect that heat is efficiently mixed by turbulence outside the viscous sublayer, so that $\lambda/\lambda_v \sim 1$. Combining with (5.6) gives the asymptotic regime $Nu \sim Ra^{1/2}$ predicted at very high Ra (e.g. Kraichnan 1962): this exponent $1/2$ can be obtained by pure dimensional analysis, assuming that the heat flux becomes independent of both viscosity and diffusivity.

5.3. *The thermal boundary layer and the relation Nu vs. Ra for* $Pr \lessdot 1$

For mercury ($Pr = 0.025$), the condition $\lambda/\lambda_v < 1$ is satisfied only for $Ra < 5 \times 10^5$, according to (5.20). Even this estimate is too large, as it is based on (5.15) which overestimates Nu by about a factor of 2 for mercury. Therefore we must instead assume that $\lambda/\lambda_v > 1$ for all Ra. This has been experimentally checked by Takeshita *et al.* (1996) at $Ra \sim 10^7$ (although by an indirect estimation of λ_v).

We therefore assume that heat undergoes ordinary diffusion with a uniform advection velocity U, yielding the classical solution for the heat equation $T(x,z) - T_{(z \to \infty)} = [T_{(z=0)} - T_{(z \to \infty)}] [1 - \text{erf} (z/2)(\kappa x/U)^{-1/2}]$, and the corresponding heat flux at the wall is $-\kappa \ \partial T/\partial z(x,0) = [T_{(z=0)} - T_{(z \to \infty)}] \ (\kappa U)^{1/2}(\pi x)^{-1/2}$. Noticing that $T_{(z=0)} - T_{(z \to \infty)} = \Delta/2$, and averaging this flux from 0 to x, yields

$$Nu_{Pr \lessdot 1} = \pi^{-1/2} (RePr)^{1/2}(x/L)^{-1/2}, \tag{5.21}$$

instead of (5.14).

Combining with (5.6), and choosing $x/L = 0.69$ yields a good fit for region II:

$$Nu_{II} = 0.92 (RaPr)^{1/5}. \tag{5.22}$$

Then (5.6) yields

$$Re_{II} = 1.95 \ Ra^{2/5}Pr^{-3/5}, \tag{5.23}$$

$$(\Delta_c/\Delta)_{II} \sim (RaPr)^{-1/5}, \tag{5.24}$$

which is consistent with our results in region II.

The law $Nu \sim Ra^{1/4}$ closely approximated in region I may be interpreted by arguments of Jones, Moore & Weiss (1976), also discussed by Kek & Muller (1993). The idea is that the thermal boundary layer reaches the bulk flow, imposing there temperature differences $\sim \Delta$, so that

$$(\Delta_c/\Delta) \sim \text{Const.}, \tag{5.25}$$

where Const. is a constant factor smaller than 1. Then the relation (5.3) for the free fall velocity implies

$$Re \sim (Ra/Pr)^{1/2}, \tag{5.26}$$

and the heat flux (5.21) in the thermal boundary layer becomes

$$Nu \sim (RaPr)^{1/4}. \tag{5.27}$$

Note that (5.6) is not satisfied by the predictions (5.26) and (5.27). This condition (5.6) is difficult to ignore from a theoretial point of view, as it can be derived from the exact relation (5.7) and the hypothesis that turbulent dissipation varies as U^3/L, which is quite reasonable for the Kolmogorov turbulence found at low Prandtl number (Cioni *et al.* 1995). Our measurements indicate that Δ_c/Δ decreases for increasing Ra (figure 9), contradicting (5.25), and our fit (4.5) for Re supports (5.6) instead of (5.26). Therefore this model disagrees with our results, in spite of the good prediction for

Nu. This conclusion must be taken with caution, however, since our measurements of Δ_c and *Re* are indirect (obtained from Δ_h and ω_p respectively). Busse & Clever (1981) also propose a law $Nu \sim Ra^{1/4}$, but without dependence on *Pr*, from a 'flywheel' assumption. Comparison between different experiments indicates instead that *Nu* increases with *Pr*.

To interpret region I, (5.21) should be corrected for shear effects. When $Nu <\sim 12$, the thermal boundary layer extends beyond the jet maximum, $\lambda > \delta$, and the approximation of a constant velocity is not good: an actual jet profile should be introduced in the heat equation. An alternative interpretation for region I is given in §5.5, using scaling laws for plumes.

At this stage we have considered only the molecular diffusion of heat, and it is important to estimate the eddy diffusivity. The logarithmic profile (5.9) is associated with an eddy diffusivity of momentum, $v_t = u_*^2/(\mathrm{d}u/\mathrm{d}z) = 0.4\, u_* z$. Using (5.10) with $Re \simeq 10^5$, we find $u_*/U \simeq 0.05$, so that $v_t \simeq 0.02\, Uz$. The eddy difusivity of heat κ_t must be of the same order, $\kappa_t \simeq 0.02 Uz$. In the thermal boundary layer, at a distance from the wall $z \sim \lambda$,

$$\kappa_t/\kappa \simeq 0.01\, Re\, Pr\, /Nu. \tag{5.28}$$

This estimate leads to a negligible eddy diffusivity in most of our experimental range: the heat exchange in the boundary layer is just controlled by the advection due to the global circulation.

However, κ_t/κ increases with *Ra*, and we expect a new regime when it reaches values of order 1. Then the thickness of the diffusive boundary layer would be controlled by the condition $\kappa_t/\kappa \sim 1$, and (5.28) then imposes $Nu \sim 0.01RePr$, corresponding (from (5.6)) to $Nu \sim 0.001(RaPr)^{1/2}$. We may reach this regime at our highest *Ra*: indeed for $Ra = 2 \times 10^9$, we find $Re = 10^5$, from the fit (4.5), and $Nu = 32$, so that (5.28) yields $\kappa_t/\kappa \sim 0.7$, possibly explaining the transition observed in region III. The Reynolds number then corresponds to the threshold for instability in a boundary layer on a flat plane, leading to sudden enhancement of turbulence, sensitive to the presence of small perturbations, consistent with our observations of a sudden and non-reproducible transition.

5.4. *The mixing zone model*

We reproduce in this subsection the arguments of Castaing *et al.* (1989) leading to the same scaling law (5.15) as Shraiman & Siggia (1990), assuming that the diffusive layer emits plumes in a so-called *mixing zone*. These plumes have a typical temperature Δ and scale λ, as they are detached sections of the diffusive layer. As they rise, the plumes supposedly become unstable and shatter, losing their identity as they reach the bulk region. The resulting finely structured fluid directly feeds the bulk flow at scale $\sim L$. This fluid has the buoyancy of a homogeneous fluid of temperature $f\Delta$, where f is the volume proportion of hot fluid at the end of the mixing zone. Matching temperature fluctuations to the bulk then imposes

$$\Delta_c \sim f\Delta. \tag{5.29}$$

The heat flux is transported by the plumes in the mixing zone, so that

$$H \sim w_h f\Delta, \tag{5.30}$$

where w_h is the plume velocity at the end of the mixing zone. We deduce from these

two relations:

$$f \sim Ra_c/Ra \sim Nu^{2/3}Ra^{-1/3}Pr^{-1/3}, \tag{5.31}$$

$$w_h\lambda/\kappa \sim 1/f \sim Nu^{-2/3}Ra^{1/3}Pr^{1/3} \tag{5.32}$$

(using (5.5) and (5.1) respectively).

The typical time τ_s between the emission of two successive plumes, at a given position on the boundary, is estimated as

$$\tau_s \sim \lambda^2/\kappa, \tag{5.33}$$

which is the time needed to rebuild the diffusive layer by heat conduction after plume emission. The typical vertical distance d_m between the two plumes is the distance $w_h\tau_s$ travelled by the first plume during the time τ_s so that, using (5.33),

$$d_m/\lambda \sim w_h\lambda/\kappa. \tag{5.34}$$

This distance d_m is also the typical thickness of the mixing zone: beyond the distance d_m from the wall, we can consider the set of plumes as an effective fluid with temperature $f\Delta$. The volume fraction can be estimated as $f \sim \lambda/d_m$, since λ is the typical size of the plume, and the result from (5.34) coincides with the independent relation (5.32). Therefore the scaling laws for velocities and temperature fluctuations in the different zones are determined, provided we have the relation between Nu and Ra.

To close the derivation, Castaing *et al.* (1989) further assume that the plumes reach a *steady velocity* w_h under the balance between buoyancy force and viscous friction, which yields, for a plume with temperature Δ and size λ

$$w_h \sim g\alpha\Delta\lambda^2/v. \tag{5.35}$$

Combining this relation with (5.32) leads again to the scaling (5.15) and its consequences (5.16)–(5.17).

5.5. *The mixing zone model adapted to low Prandtl numbers*

The estimate (5.35) is not justified at low Pr: the plume cannot reach a steady velocity. Indeed the time τ_a for the plume to reach this velocity is equal to the final velocity (5.35) divided by the initial acceleration $\alpha g\Delta$, so $\tau_a = \lambda^2/v$, and comparing with (5.33),

$$\tau_a/\tau_s \sim Pr^{-1}. \tag{5.36}$$

Thus the assumption (5.35) that the plumes reach a constant velocity cannot hold for low Pr (in fact Castaing *et al.* 1989 propose their model only for $Pr \sim 1$, without attempting to derive the dependence on Pr). For low Pr, we assume instead that the plume is *steadily accelerating* in the whole mixing zone, with acceleration $g\alpha\Delta$, so that

$$w_h \sim g\alpha\Delta\tau_s \sim g\alpha\Delta\lambda^2/\kappa, \tag{5.37}$$

instead of (5.35) (we have used (5.33) to get the second equality), yielding

$$Nu_{Pr<0.3} = 0.25\,(RaPr)^{2/7}. \tag{5.38}$$

The coefficient 0.25 is obtained by a fit to our experimental results in mercury. The expression (5.38) is represented in figure 2(*b*) by the dashed line. The intersection with the value of Nu for $Pr \sim 1$ occurs for $Pr \simeq 0.3$. We thus expect that the low-Pr regime obtains for $Pr \leqslant 0.3$. The parameter $RaPr$ depends only on the thermal

diffusivity, so that the heat flux becomes independent of viscosity at low Prandtl number, which is reasonable, as diffusivity then dominates viscosity.

The other scaling laws for $Pr < 0.3$ are then readily deduced from (5.5) and (5.6):

$$Re_{Pr<0.3} \sim Pr^{-1}(RaPr)^{3/7}, \tag{5.39}$$

$$(\Delta_c/\Delta)_{Pr<0.3} \sim (RaPr)^{-1/7}. \tag{5.40}$$

6. Conclusions

For mercury, the Nusselt number is about half that for fluids with $Pr \sim 1$, at the same Ra. This dependence on Pr agrees with the model of Kraichnan (1962), predicting $Ra \sim Pr^{1/3}$ for $Pr < 0.1$ and a constant for $Pr > 0.1$ (at a given Ra). More recent models of Castaing *et al.* (1989) and Siggia (1990) predict a variation in Pr with the opposite sign! However these models were aimed to interpret experimental results at $Pr \sim 1$, in particular the law $Nu \sim Ra^{2/7}$ rather than the 'classical' law $Nu \sim Ra^{1/3}$. We have revisited these models and found that they are inconsistent for low Pr, and we propose appropriate modifications in §5. Even at $Pr \sim 1$, the predicted dependence of Ra as $Pr^{-1/7}$ seems incorrect. Comparison of various experiments supports instead the prediction of Kraichnan (1962) of a constant Nu (as a function of Pr). The Pr dependence therefore puts the different theories into perspective, and more studies at different Pr should be undertaken.

For the dependence of Nu on Ra, we distinguish different ranges of Ra. In region I, for $Ra < 4.5 \times 10^8$, we find a fit for $Ra^{0.26}$ in remarkable agreement with the result of Rossby (1969) at lower Ra. The exponent differs from $1/3$, and is close to the $2/7$ observed in helium, even decreasing to ~ 0.2 in region II reached for $Ra > 4.5 \times 10^8$. Finally we have observed a second transition at $Ra = 2 \times 10^9$, which we interpret as the onset of turbulent transfers in the thermal boundary layer, perhaps, leading to the asymptotic regime of convection with $Nu \sim Ra^{1/2}$. Experiments at higher Ra are needed to confirm and study this transition.

The spontaneous formation of a global circulation is observed in mercury as at $Pr \sim 1$. A temperature oscillation in the plate is associated with this global circulation, as with fluids at $Pr \sim 1$. The frequency of this oscillation is proportional to the global circulation velocity in both cases. This global circulation tends to fluctuate in strength around a mean value, never disappearing. It also randomly rotates in azimuth, with reversals between two preferred directions, and fluctuations of smaller extent with a time scale of a few minutes. It is still an open question whether this dynamics is specific to low Prandtl number.

The scaling of global circulation velocity with Ra in mercury agrees with the free fall relation (5.6), while a discrepancy is observed for helium. We interpret this difference by the different dynamics revealed by time spectra: the scaling (5.6) corresponds to energy dissipation by the Kolmogorov turbulence that we have observed in mercury. A different dissipation law is obtained with the Bolgiano–Oboukhov dynamics detected at $Pr \sim 1$, as discussed in Appendix A.

However the main difference is in the boundary layer structure. As shown experimentally by Takeshita *et al.* (1996), the viscous boundary layer is nested inside the thermal boundary layer in mercury, unlike in experiments performed at $Pr \sim 1$. We justify this difference in §5 by estimating the thickness of these two boundary layers for different Pr: we consider a model involving a direct coupling between a big convective cell and a thermal boundary layer. The velocity of this convective cell

is given by the free fall relation (5.6). For $Pr \sim 1$ (and Ra not too large, according to (5.20)), the thermal boundary layer is inside the viscous one, which corresponds to the model of Shraiman & Siggia (1990) (but we have changed prefactors to fit better recent experimental results). The opposite case obtains at low Pr, and a law $Nu \sim (RaPr)^{1/5}$ is expected. This analysis interprets region II behaviour, and may explain the transition that we observe at $Ra \simeq 2 \times 10^9$ in mercury (region III). At this value of Ra two effects are expected: the boundary layer reaches a Reynolds number at which it becomes intrinsically turbulent, and turbulent heat transport begins to dominate over diffusion near the boundary (according to (5.28)). Beyond this threshold an asymptotic regime $Nu \sim (RaPr)^{1/2}$ is expected.

Although this model provides a good interpretation of regions II and III, it does not explain the scaling of Nu in region I. The same boundary layer analysis yields a much better scaling $Nu \sim (RaPr)^{1/4}$ if we use the velocity (5.26) instead of (5.6), following Jones *et al.* (1976). However (5.6) is in better agreement with the experiments.

As an alternative approach, we have considered the mixing zone model of Castaing *et al.* (1989), §5.4. In this model the plumes reach a steady velocity balancing buoyancy and viscous friction. Instead, at low Pr, plumes are accelerated steadily until they mix into the bulk flow, leading to $Nu \sim (RaPr)^{2/7}$ (§5.5), in reasonable agreement with experimental results in region I. Nu is then smaller for smaller Pr, in agreement with the experiments.

The Chicago experiments (Castaing *et al.* 1989) displayed beautiful power laws, interpreted in terms of general scaling arguments involving plumes. In his review paper, Siggia (1994) stressed, however, that we should not forget the underlying fluid mechanics. In his model, buoyancy drives the global circulation, but heat transfers are controlled by the development of a thermal boundary, with temperature transported by the global circulation like a passive tracor. The two approaches give similar results at $Pr \sim 1$, and it is not clear which description applies, or whether they just consider different aspects of the same physics. Ciliberto *et al.* (1996) have shown that heat transfers are unchanged when the global circulation is suppressed by screens in a water experiment, supporting plumes model. In the case of low Pr, two models, discussed in §5.3 and §5.5 respectively, give different results. The plume model provides a good interpretation of region I, while the boundary layer approach interprets of regions II and III. However, we do not see the link between these different approaches.

Appendix A. Turbulent energy dissipation in buoyancy-controlled turbulence

In mercury, Cioni *et al.* (1995) showed that temperature fluctuations in the bulk behave like a passive scalar in ordinary turbulence. Therefore the rate of kinetic energy dissipation is expected to vary as U^3/L. In contrast, temperature spectra varying as $k^{-1.4}$ have been measured in helium and water (from time spectra, using a Taylor hypothesis). Such spectra have been related to Bolgiano–Oboukhov dynamics, controlled by buoyancy effects (Wu *et al.* 1990; L'vov 1991; Chilla *et al.* 1993*b*; Benzi *et al.* 1994). A different scaling for the dissipation is then expected.

Both temperature fluctuations and kinetic energy are assumed to be introduced at

some integral scale assumed of order L, transferred to small scales by turbulence, and dissipated by diffusive and viscous effects respectively. The rate of kinetic energy dissipation $\epsilon = \nu \langle |\nabla u|^2 \rangle$ is given from the Boussinesq equation by (5.7). Similarly, the rate of dissipation for the temperature variance $N = \kappa \langle |\nabla T|^2 \rangle$ is given by averaging the heat equation (multiplied by T):

$$Nu = \langle |\nabla T|^2 \rangle L^2 / \Delta^2. \tag{A 1}$$

At each scale r, the r.m.s. temperature fluctuations $\theta^2(r)$ are transferred to smaller scales by the typical velocity fluctuations $u'(r)$ at this scale. The time for this process is $r/u'(r)$, so the local rate of transfer is $\theta^2 u'(r)/r$. Assuming this rate is constant and equal to N yields

$$u'(r)\,\theta^2(r)\,/\,r = N. \tag{A 2}$$

The same argument for a conserved kinetic energy u'^2 leads to the Kolmogorov scaling $u' \sim \epsilon^{1/3} r^{1/3}$. In this case (A 2) yields the Kolmogorov scaling for a passive scalar $\theta(r) \sim N^{1/2} \epsilon^{-1/6} r^{1/3}$.

In Bolgiano scaling, the kinetic energy is not conserved in the cascade, but is supplied from potential energy. Velocity and temperature are then related by the free fall relation at each scale:

$$u'(r) \sim (\alpha g\, \theta\, r)^{1/2}. \tag{A 3}$$

The combination of (A 2) and (A 3) gives the Bolgiano scaling:

$$u'(r) \sim (\alpha g)^{2/5}\, N^{1/5}\, r^{3/5}, \qquad \theta(r) \sim (\alpha g)^{-1/5}\, N^{2/5}\, r^{1/5}. \tag{A 4}$$

The Bolgiano and Kolmogorov scalings cross at the Bolgiano scale:

$$L_b = \epsilon^{5/4}\, N^{-3/4}\, (g\alpha)^{-3/2}. \tag{A 5}$$

Bolgiano scaling is expected for $r > L_b$ while Kolmogorov scaling is expected for $r < L_b$. The scale L_b can be calculated from the experimental parameters using (5.7) and (A 1), following Chilla *et al.* (1993a), yielding

$$L_b/L = Nu^{1/2}\, Ra^{-1/4}\, Pr^{-1/4}. \tag{A 6}$$

Bolgiano scaling dominates for large Pr (L_b small), while the Kolmogorov scaling prevails for small Pr, in agreement with the different behaviour observed in experiments and numerical simulations at $Pr \sim 1$ and in mercury (Cioni *et al.* 1995). The existence of the crossover scale L_b was not really demonstrated in the experiments, due to the limited size of the inertial range. However, we shall consider the influence of this scale to relate the energy dissipation to the convective velocity U.

In Kolmogorov scaling, the energy dissipation rate ϵ is controlled by the integral scale L, $\epsilon \sim U^3/L$. In Bolgiano dynamics, we must replace this scale by the Bolgiano scale, where the Kolmogorov cascade begins:

$$\epsilon = u'(L_b)^3\,/\,L_b. \tag{A 7}$$

We can relate $u'(L_b)$ to the energy at the energy-containing scale L by (A 4)

$$u'(L_b)/U \sim (L_b/L)^{3/5}. \tag{A 8}$$

Then, (A 7) yields

$$\epsilon \sim (L_b/L)^{4/5}\, U^3\,/\,L, \tag{A 9}$$

which can be related to the experimental parameters by (A 6):

$$\epsilon \sim Nu^{2/5}\, Ra^{-1/5}\, Pr^{-1/5}\, U^3/L. \tag{A 10}$$

Then (5.7) yields

$$Re \sim Nu^{1/5} \, Ra^{2/5} \, Pr^{-3/5}, \tag{A 11}$$

instead of (5.6). Introducing a law $Ra \sim Nu^{2/7}$, yields an exponent $16/35 \simeq 0.46$ for Re vs. Ra, instead of the exponent $3/7 \simeq 0.43$ obtained with Kolmogorov scaling. The correction is very close to the result obtained by Siggia (1994) with the logarithmic boundary layer, which was observed to fit well the experiments in helium (taking into account also the dependence on Pr). However, this correction applies only for $Pr \sim 1$, and not for mercury, in agreement with our measurements.

Appendix B. The thermal condition at the bottom plate

The boundary conditions at the top and bottom of the cell are not simple. Indeed the copper plates are not able to set a uniform temperature along each plate, as often assumed for Rayleigh–Bénard convection, so the heat transfers in the plates must be considered.

Suppose that the plate is at temperature $T_W(x, y, t)$, while the fluid in the bulk is at temperature $T_F(x, y, t)$. Assume that the plate has small thickness $e \ll L$, so that its temperature is independent of the vertical coordinate. We can then write an equation for heat conduction in the horizontal plane of the plate, with a (uniform) heat source S due to the electrical heating power, and a local flux $H^*(x, y)$ toward the fluid:

$$eC_W \, \partial T_W / \partial t \; = \; eC_W \, \kappa_W \nabla^2 T_W \; - \; H^* \; + \; S, \tag{B 1}$$

where C_W denotes the heat capacity (per unit volume) for the bottom plate, and κ_W its thermal diffusivity.

The heat flux $H^* = HC_F$ is given by an experimental relationship of form $Nu \sim Ra^{n-1}$ (n real). Assume this relationship is valid *locally*, with Nu and Ra calculated from the local flux H and $\Delta = 2(T_W - T_F)$ (considering that the total temperature difference Δ is concentrated in the two boundary layers). This leads to

$$H(x, y, t) \; = \; h \, (T_W - T_F)^n, \tag{B 2}$$

where h is a constant related to the prefactor in the relation $Nu \sim Ra^{n-1}$. Assume that T_W and T_F fluctuate around their mean values over the plate (denoted by $\langle . \rangle$), $T_W = \langle T_W \rangle + \theta_W(x, y, t)$ and $T_F = \langle T_F \rangle + \theta_F(x, y, t)$. Expanding the heat flux (B 2) for small fluctuations leads to

$$H \; \simeq \; \langle H \rangle \; + \; n \langle H \rangle (\theta_W - \theta_F) / (\langle T_W \rangle - \langle T_F \rangle). \tag{B 3}$$

We consider also a spatial modulation of the flux associated with the development of the thermal boundary layer, occurring even when $T_W - T_F$ is uniform. In this case we write

$$H(x, y, t) \; = \; \langle H \rangle (1 + f(x, y)). \tag{B 4}$$

For an ordinary thermal boundary layer developing along x, we have

$$1 + f(x, y) \; = \; x^{-1/2} / \langle x^{-1/2} \rangle \; \simeq \; 0.5 (x/L)^{-1/2}, \tag{B 5}$$

corresponding to the growth of the boundary layer thickness as $(\kappa x)^{1/2}$ (from a somewhat arbitrary origin at the edge of the plate).

We expect that both effects occur together, and superpose them for small modulations, writing

$$H(x, y, t) \; = \; \langle H \rangle \, [1 \; + \; n(\theta_W - \theta_F) / (\langle T_W \rangle - \langle T_F \rangle) \; + \; f(x, y)]. \tag{B 6}$$

The mean flux $\langle H \rangle C_F$ is balanced by the heat source S, so the heat equation (B 1) becomes

$$(L^2 \kappa_W^{-1}) \, \partial \theta_W / \partial t = L^2 \nabla^2 \theta_W - 2B \, Nu \, [n(\theta_W - \theta_F) + (\langle T_W \rangle - \langle T_F \rangle) f(x, y)], \quad \text{(B 7)}$$

where we have used $\Delta = 2(\langle T_W \rangle - \langle T_F \rangle)$, and introduced the non-dimensional parameter

$$B = \frac{C_F \kappa}{C_W \kappa_W} \frac{L}{e}. \quad \text{(B 8)}$$

For our copper plate with $e = 2$ cm and mercury, we find $B = 0.226$.

Consider a dipolar structure which is an eigenfunction of the Laplacian on the plate:

$$\theta_F = \Theta_F(t) \, J_1(kr) \cos \phi, \quad \nabla^2 \theta_F = -k^2 \theta_F, \quad \text{(B 9)}$$

where J_1 is the Bessel function of first kind of order 1. The boundary condition of zero radial flux at $r = L/2$ implies that $J_1'(kL/2) = 0$, corresponding to $kL/2 \simeq 1.84$, the first zero of J_1'.

We introduce (B 9) in the heat equation (B 7), and assume $f(x, y) = F J_1(kr) \cos \phi$ has the same dipolar structure (otherwise we should expand it in Bessel functions), yielding $\theta_W = \Theta_W(t) J_1(kr) \cos \phi$ with

$$[L^2 \kappa_W^{-1} \partial / \partial t + k^2 L^2 + 2B \, n \, Nu] \Theta_W = 2B \, n \, Nu \, \Theta_F - 2B \, Nu \, F \, (\langle T_W \rangle - \langle T_F \rangle). \quad \text{(B 10)}$$

The thermal inertia time of the plate is (for the dipolar mode) $L^2 \kappa_W^{-1} (kL)^{-2} = 30$ s. We consider fluctuations on longer time scales, so we can neglect the time derivative in (B 10). Then (B 10) yields

$$\Theta_F = \left[1 + \frac{6.77}{BnNu} \right] \Theta_W + \frac{F\Delta}{2n}. \quad \text{(B 11)}$$

We measure the crest-to-crest amplitude Δ_h at radius $r = 0.23L$, so that $\Delta_h = 2\Theta_W J_1(kr)$. The coefficient F can be estimated from (B 5), which yields $f = -0.04$ at $x = 0.5L - r$ and $f = -0.49$ at $x = 0.5L + r$. The crest-to-crest amplitude of f is therefore 0.45, so that $F J_1(kr) = -0.23$. Therefore the correspondance between the amplitude Δ_h and the corresponding amplitude Δ_c in the fluid is given by

$$\Delta_c / \Delta \simeq \left[1 + \frac{6.77}{BnNu} \right] \Delta_h / \Delta - 0.2. \quad \text{(B 12)}$$

Equation (B 12) indicates two sources for the dipolar structure: the presence of a dipolar structure Θ_F in the bulk, and the development of the thermal boundary layer. Both effects are filtered by the thermal conduction in the plate. At low Nu, this filtering is efficient, due to the high conductivity of copper in comparison with mercury, so we are close to a condition of uniform temperature at the wall. However, as Nu increases, the 'turbulent conductivity' of the fluid increases, and we tend to a condition of constant flux (for the dipolar mode). For water the conductivity is 13 time smaller ($B = 0.017$), so the condition of uniform temperature in the plate is better satisfied.

REFERENCES

BARTOLONI, A., BATTISTA, C., CABASINO, S., PAOLUCCI, P. S., PECH, J., SARNO, R., TODESCO, G. M., TORELLI, M., TROSS, W., VICINI, P., BENZI, R., CABIBBO, N., MASSAIOLI, F. & TRIPICCIONE, R. 1993 LBE simulations of Rayleigh-Benard convection on the APE100 parallel processor. *Intl J. Mod. Phys.* C **4**, 993–1007.

BELMONTE, A., TILGNER, A. & LIBCHABER, A. Temperature and velocity boundary layers in turbulent convection. *Phys. Rev.* E **50**, 269–279.

BENZI, R., TRIPICCIONE, R., MASSAIOLI, F., SUCCI, S. & CILIBERTO, S. 1994 On the scaling of the velocity and temperature structure functions in Rayleigh-Benard convection. *Europhys. Lett.* **25**, 341–346.

BOLDGIANO, R. 1959 Turbulent spectra in a stably stratified atmosphere. *J. Geophys. Res. SSSR Ser. Georgr. e Geifiz.* **64**, 2226.

BUSSE, F. H. & CLEVER, R. M. 1981 An asymptotic model of two-dimensional convection in the limit of low Prandtl number. *J. Fluid Mech.* **102**, 75–83.

CASTAING, B., GUNARATNE, G., HESLOT, F., KADANOFF, L., LIBCHABER, A., THOMAE, S., WU, X., ZALESKI, S. & ZANETTI, G. 1989 Scaling of hard thermal turbulence in Rayleigh-Bénard convection. *J. Fluid Mech.* **204**, 1–29.

CHAVANNE, X., CHILLA, F., CHABAUD, B., CASTAING, B., CHAUSSY, J. & HÉBRAL, B. 1996 High Rayleigh number convection with gaseous helium at low temperature. *J. Low Temp. Phys.* (submitted).

CHILLA, F., CILIBERTO, S., INNOCENTI, C. & PAMPALONI, E. 1993a Boundary layer and scaling properties in turbulent thermal convection. *Il Nuovo Cimento* **15D**, 1229–1249.

CHILLA, F., CILIBERTO, S., INNOCENTI, C. & PAMPALONI, E. 1993b Spectra of local and averaged scalar fields in turbulence. *Europhys. Lett.* **22**, 23–28.

CHU, T. Y. & GOLDSTEIN, R. J. 1973 Turbulent natural convection in a horizontal water layer heated from below. *J. Fluid Mech.* **60**, 141–159.

CILIBERTO, S., CIONI, S. & LAROCHE, C. 1996 Large scale flow properties of turbulent thermal convection. *Phys. Rev.* E **54**, 5901–5905.

CIONI, S., CILIBERTO, S. & SOMMERIA, J. 1995 Temperature structure functions in turbulent convection at low Prandtl number. *Europhys. Lett.* **32**, 413–418.

CIONI, S., CILIBERTO, S. & SOMMERIA J. 1996 Experimental study of High-Rayleigh-Bénard convection in mercury and water. *Dyn. Atmos. Oceans* **24**, 117–127.

FITZJARRALD, D. E. 1976 An experimental study of turbulent convection in air. *J. Fluid Mech.* **73**, 693–719.

GARON, A. M. & GOLDSTEIN, R. J. 1973 Velocity and heat transfer measurements in thermal convection. *Phys. Fluids* **16**, 1818–1825.

GLOBE, S. & DROPKIN, D. 1959 Natural-convection heat transfer in liquids confined by two horizontal plates and heated from below. *J. Heat Transfer* **31**, 24–28.

GOLDSTEIN, R. J., CHIANG, H. D. & SEE, D. L. 1990 High-Rayleigh-number convection in a horizontal enclosure. *J. Fluid Mech.* **213**, 111–126.

GOLDSTEIN, R. J. & TOKUDA, S. 1980 Heat transfer by thermal convection at high Rayleigh numbers. *Intl J. Heat Mass Transfer* **23**, 738–740.

JONES, C. A., MOORE, D. R. & WEISS, N. O. 1973 Axisymmetric convection in a cylinder. *J. Fluid Mech.* **73**, 353–388.

KEK, V. & MULLER, U. 1993 Low Prandtl number convection in layers heated from below. *Intl J. Heat Mass Transfer* **36**, 2795–2804.

KERR, B. 1996 Rayleigh number scaling in numerical convection. *J. Fluid Mech.* **310**, 139–179.

KRAICHNAN, R. 1962 Turbulent thermal convection at arbitrary Prandtl number. *Phys. Fluids* **5**, 1374–1389.

KRISHNAMURTI, R. & HOWARD, L. N. 1981 Large-scale flow generation in turbulent convection. *Proc. Natl Acad. Sci. USA* **78**, 1981–1985.

L'VOV, V. S. 1991 Spectra of velocity and temperature fluctuations with constant entropy flux of fully developed free convective turbulence. *Phys. Rev. Lett.* **67**, 687–690.

ROSSBY, H. T. 1969 A study of Bénard convection with and without rotation. *J. Fluid Mech.* **36**, 309–335.

SANO, M., WU, X. Z. & LIBCHABER, A. 1989 Turbulence in helium-gas free convection. *Phys. Rev.* A **40**, 6421.

SCHLICHTING, H. 1968 *Boundary-Layer Theory*. Mc Graw-Hill.

SHRAIMAN, B. I. & SIGGIA, E. D. 1990 Heat transport in high-Rayleigh-number convection. *Phys. Rev.* A **42**, 3650.

SIGGIA, E. D. 1994 High Rayleigh number convection. *Ann. Rev. Fluid Mech.* **26**, 137–168.

TAKESHITA, T., SEGAWA, T., GLAZIER, J. A. & SANO, M. 1996 Thermal turbulence in mercury. *Phys. Rev Lett*. **76**, 1465–1468.

TANAKA, H. & MIYATA, H. 1980 Turbulent natural convection in a horizontal water layer heated from below. *Intl J. Heat Mass Transfer* **23**, 1273–1281.

THRELFALL, D. C. 1975 Free convection in low temperature gaseous helium. *J. Fluid Mech.* **67**, 17–28.

TILGNER, A., BELMONTE, A. & LIBCHABER, A. 1993 Temperature and velocity profiles of turbulent convection in water. *Phys. Rev.* E **47**, 2253–2256.

VILLERMEAUX, E. 1995 Memory-induced low frequency oscillations in closed convection boxes. *Phys. Rev. Lett.* **75**, 4618–4621.

WU, X., KADANOFF, L., LIBCHABER, A. & SANO, M. 1990 Frequency power spectrum of fluctuations in free convection. *Phys. Rev. Lett.* **64**, 2140–2143.